Channel Knowledge Map-Enabled 6D Movable Antenna Systems With Kinematic Constraints: A Manifold Optimization Approach

Nan Cheng, *Senior Member, IEEE*, Shuangyu Yang, *Graduate Student Member, IEEE*, Ruijin Sun, *Member, IEEE*, Zhisheng Yin, *Member, IEEE*, Xiaodan Shao, *Member, IEEE*, Weihua Zhuang, *Fellow, IEEE*, and Xuemin Shen, *Fellow, IEEE*

***Abstract*—Six-dimensional movable antenna (6DMA) offers a potential solution to enhance wireless transmission performance by physically reconfiguring antenna positions and orientations. However, prevailing snapshot-based reactive methods are ill-suited for continuously tracking mobile user equipments (UEs) due to their neglect of antenna kinematic constraints and system latency. To address these limitations, in this paper, we propose a proactive approach by modeling UE tracking as a single, long-term 6DMA trajectory optimization problem to maximize sum spectral efficiency. Leveraging a channel knowledge map (CKM) for predictive data, our model holistically incorporates the system's complex kinematics and physical constraints, including velocity limits and safety distances, to ensure a physically feasible trajectory. To solve this high-dimensional, non-convex problem, we develop a novel manifold optimization algorithm. This method maps the antenna's rotational states onto the SO(3) Lie group and employs an adaptive penalty measure with tangent space backpropagation for an efficient solution. Simulation results demonstrate our approach significantly enhances sum spectral efficiency over benchmarks, while ensuring continuous and physically feasible antenna trajectories.**

***Index Terms*—6D movable antenna, trajectory optimization, proactive tracking, channel knowledge map, manifold optimization, kinematic constraints, spectral efficiency.**

I. Introduction

TO MEET future wireless capacity demands, multiple-input multiple-output (MIMO) technology has been crucial, evolving into massive and extremely large-scale systems to enhance spectral efficiency. However, the reliance on fixed-position antennas (FPAs) in next-generation systems, especially at higher frequencies with large arrays for complex scenarios [1], [2], has led to prohibitive costs and diminishing returns. This has spurred research into more efficient ways to utilize spatial degrees of freedom (DoFs) [3].

Movable antenna (MA) techniques have emerged as a promising solution. Unlike FPAs, MAs can physically change their position to find better channel conditions [4], [5]. The six-dimensional movable antenna (6DMA) concept extends this by adding 3D rotational capabilities to the 3D translational movement [6], [7]. These six DoFs allow a base station (BS) to finely adjust its antenna array's geometry and orientation, enhancing beamforming and spatial multiplexing without adding more antennas [8]. The core idea of MA/6DMA is optimizing antenna position and orientation alongside traditional communication parameters. Research in this area includes joint optimization of antenna poses and beamforming to maximize sum rate [9], [10] or minimize transmit power [11]. This has also been applied to integrated sensing and communication [12], [13] and physical layer security [14]. Additionally, methods for channel estimation across all possible antenna poses have been developed [15].

Despite its promising applications, existing studies on 6DMA mainly focus on a snapshot-based static optimization paradigm. This approach seeks to find a single, optimal fixed antenna pose for a given time instant, conditioned on instantaneous channel state information (CSI). This reactive strategy, however, is inherently myopic. It optimizes each state in isolation, disregarding the physical constraints of motion and the long-term performance of the resulting trajectory. While its effectiveness has been validated in low-mobility or quasi-static channel scenarios [10], [16]. The rise of high-mobility, mission-critical applications, such as drone tracking [17] and connected vehicles [18], demands a paradigm shift from reactive adjustments to proactive, long-term trajectory optimization to ensure the required continuous, high-fidelity service. A primary consideration is ensuring kinematic feasibility, a factor not typically at the forefront of the prevailing optimization paradigm. This approach, centered on finding an optimal pose for an instantaneous channel state [6], [16], can be applied sequentially to dynamic tracking tasks. However, this may result in a myopic optimization, as the formulation does not explicitly incorporate kinematic constraints or the impact of a current decision on future movements. By optimizing each state in isolation, the method could yield a

Received 22 August 2025; revised 28 October 2025; accepted 13 December 2025. Date of publication 26 December 2025; date of current version 12 January 2026. This work was supported in part by the National Key Research and Development Program of China under Grant 2024YFB907500 and in part by the National Natural Science Foundation of China (NSFC) under Grant 62201414. The associate editor coordinating the review of this article and approving it for publication was G. Zhu. *(Corresponding author: Ruijin Sun.)*

Nan Cheng, Shuangyu Yang, Ruijin Sun, and Zhisheng Yin are with the State Key Laboratory of ISN, the School of Telecommunications Engineering, Xidian University, Xi'an 710071, China (e-mail: nancheng@xidian.edu.cn; ysy@stu.xidian.edu.cn; sunruijin@xidian.edu.cn; zsyin@xidian.edu.cn).

Xiaodan Shao, Weihua Zhuang, and Xuemin Shen are with the Department of Electrical and Computer Engineering, University of Waterloo, Waterloo, ON N2L 3G1, Canada (e-mail: x6shao@uwaterloo.ca; wzhuang@uwaterloo.ca; sshen@uwaterloo.ca).

Digital Object Identifier 10.1109/TWC.2025.3645480

sequence of poses that, while individually optimal, may form a trajectory that is kinematically challenging to execute or less efficient over the long term. A second challenge relates to channel information latency. In dynamic tracking scenarios, the conventional 'measure-then-optimize' reactive control loop is subject to inherent delays from both channel estimation and decision-making. By the time the system has estimated the channel, computed the optimal pose, and enacted the movement, the CSI underpinning the decision may no longer accurately reflect the current channel state. This potential mismatch can compromise link quality. While leveraging long-term statistical channel information offers a way to mitigate this latency [19], it represents a trade-off. For systems with limited mechanical agility or those serving a large user equipment (UE) population, this strategy is practical. However, for a 6DMA system with sufficient mobility to track a small number of UEs, this approach may not fully leverage the real-time adaptability that is a key advantage of movable antennas, as the solution is optimized for an average condition rather than the specific instant.

Motivated by these observations, this paper explores a shift in perspective from discrete, snapshot-based optimization to a more holistic, proactive long-term 6DMA trajectory optimization. This approach aims to address the challenge of kinematic feasibility by formulating the entire trajectory as a single, coherent problem, thereby enabling the planning of smooth, continuous, and physically realizable movements. The realization of this proactive paradigm is facilitated by a channel knowledge map (CKM) [20], which allows for the predictive acquisition of channel information over a service horizon by mapping geographic locations to channel parameters. Building on this predictive capability, we develop a novel optimization framework. First, we establish a high-fidelity kinematic model using Rodrigues' rotation formula to explicitly characterize the channel's dependence on the antenna's six DoFs. This model accurately captures the cumulative effects of control actions and is integrated with a suite of practical physical constraints to ensure engineering viability. While this model offers a more accurate representation, it leads to a high-dimensional, non-convex optimization problem that can be challenging for conventional solvers. Second, to address this problem, we propose a manifold optimization algorithm. By treating the antenna's rotational parameters as elements on the special orthogonal group SO(3), our method is designed to efficiently compute high-quality and engineering-feasible trajectories. The main contributions of this paper are summarized as follows.

- We formulate the task of proactive tracking coverage for mobile UEs as a long term 6DMA trajectory optimization problem aimed at maximizing the sum spectral efficiency over the service horizon. A key feature of this problem model is its comprehensive consideration of the complex kinematics of the 6DMA system, for which we propose a novel long-period kinematic model using Rodrigues' rotation formula to accurately model the channel's dependence on the antenna's six DoFs. We systematically integrate a series of critical physical feasibility constraints, including maximum angular velocity, displacement limits, minimum safe distance between antennas, and the avoidance of signal self-reflection, thereby ensuring the engineering viability of the optimization results.
- To address the high dimensionality and non-convexity of the formulated problem, we propose a solution framework based on manifold optimization. This method optimizes the antenna's rotational parameters directly on the special orthogonal group SO(3). The superiority of this approach is its ability to intrinsically satisfy the orthogonality constraints of rotation matrices, thus naturally circumventing the singularity issues and complex trigonometric constraints associated with traditional parameterizations. This allows the optimization process to be conducted in the variable's natural geometric space, enhancing the stability and efficiency of the algorithm.
- Within the manifold optimization framework, we design a novel iterative algorithm. This algorithm computes the Riemannian gradient via backpropagation on the tangent space and incorporates an adaptive penalty measure to handle the complex geometric and kinematic constraints. This method ensures that constraints are met while stably guiding the algorithm toward high-quality solutions.
- We conducted extensive numerical simulations to comprehensively validate the effectiveness and practical feasibility of our proposed framework. The results demonstrate that our proactive 6DMA trajectory optimization approach significantly enhances the sum spectral efficiency compared to benchmark schemes. Crucially, this performance gain is achieved while strictly adhering to all kinematic and physical constraints, thereby validating the superior performance and engineering viability of our solution.

Notation: Bold lowercase and uppercase letters denote vectors and matrices, respectively. Calligraphic letters denote sets. For a matrix $\mathbf{A}$, its transpose, conjugate transpose, trace, and determinant are denoted by $\mathbf{A}^T$, $\mathbf{A}^H$, $\mathrm{tr}(\mathbf{A})$, and $\det(\mathbf{A})$. For two vectors $\mathbf{a}$ and $\mathbf{b}$, their dot product is denoted by $\mathbf{a} \cdot \mathbf{b}$. The Euclidean norm of a vector and the absolute value of a scalar are represented by $\|\cdot\|$ and $|\cdot|$, respectively. $\mathbf{I}_M$ is the $M \times M$ identity matrix. SO(3) denotes the special orthogonal group of 3×3 rotation matrices, with $\mathfrak{so}(3)$ as its Lie algebra. The operator $(\cdot)^\times$ maps a vector $\mathbf{u} \in \mathbb{R}^3$ to its skew-symmetric cross-product matrix. The exponential map, logarithm map, group composition, tangent space addition, and manifold subtraction are denoted by $\exp(\cdot)$, $\mathrm{Log}(\cdot)$, $\circ$, $\oplus$, and $\ominus$, respectively.

II. System Model

In this section, we first introduce the 6DMA-BS model under consideration for uplink communication from mobile UEs. Subsequently, we present the UE mobility model, the antenna mobility model, and their corresponding channel models.

A. 6DMA-BS Model

As illustrated in Fig. 1, we consider a multiuser uplink communication system where a BS serves K mobile UEs

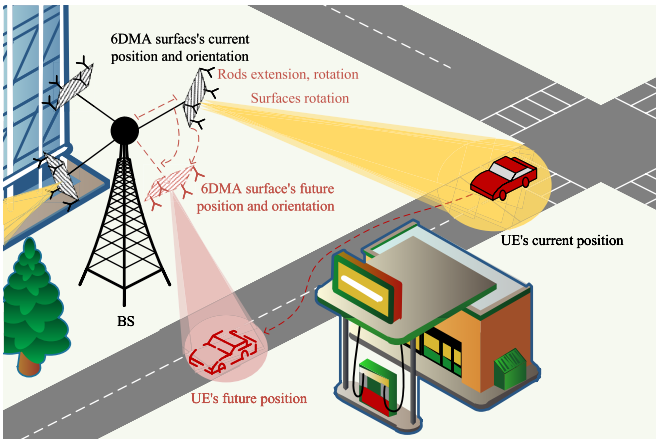

Fig. 1. An illustrative scenario of a 6DMA-enabled BS performing proactive UE tracking. Through long-term trajectory optimization, the BS smoothly adjusts its antenna position and orientation, ensuring continuous and robust communication links along the UEs' trajectories.

over service horizon T. This duration is discretized uniformly into M time slots, indexed by the set $\mathcal{T} = \{1, 2, \ldots, M\}$, each with a length of $\Delta t = T/M$. The BS is equipped with A 6DMA surfaces, indexed by $a \in \mathcal{A} = \{1, 2, \ldots, A\}$. Each surface constitutes a uniform planar array (UPA) with N antenna elements indexed by $n \in \mathcal{N}_a = \{1, 2, \ldots, N\}$. Each UE, indexed by $k \in \mathcal{K} = \{1, 2, \ldots, K\}$, is equipped with a single fixed-position antenna. A key assumption in our model is that the spatiotemporal trajectories of all UEs are accurately known a priori at the BS. The spatial configuration of each 6DMA surface, including its 3D position and orientation, can be dynamically reconfigured across time slots to enhance channel conditions for trajectory-aware service provision. Specifically, each 6DMA surface installed at the BS is connected to the central processing unit (CPU) located at the BS through L extendable and rotatable supporting rods embedded with flexible wires. The set of supporting rods is denoted by $\mathcal{L} = \{1, 2, \ldots, L\}$. Each supporting rod holds one 6DMA surface, and its end is connected to that surface through a universal joint, where the indices are in one-to-one correspondence. By controlling the extension, rotation, and 3D movement of these supporting rods through the CPU, the position coordinates of each 6DMA surface in the 3D space and the deflection angle relative to the plane normal can be flexibly adjusted. This system supports the precise position adjustment and attitude control of the 6DMA surfaces in the omnidirectional space, providing a hardware foundation for the dynamic optimization of the wireless transmission link.

Next, we discuss the effect of rod rotation on antenna position. Taking the connection point between the BS and the antenna supporting rod as the origin $\mathbf{q}_0^{\mathrm{b}} = (0, 0, 0)^{\mathrm{T}}$, we construct a global cartesian coordinate system (CCS). At time slot t, the position of the a-th 6DMA surface center, which corresponds to the terminal end of the l-th rod, is denoted by $\mathbf{q}_l^{\mathrm{b}}[t] = (x_l, y_l, z_l)^{\mathrm{T}}$, where x_l, y_l, and z_l are the coordinates of the 6DMA surface along the x, y, and z axes of the global CCS, respectively. The rotation axis of the l-th supporting rod is defined by unit vector $\mathbf{u}_l = (u_x, u_y, u_z)^{\mathrm{T}}$. In this global coordinate system, the angular velocity of rotation about this axis is denoted as $\omega_l[t]$, and the corresponding rotation angle, $\theta_l[t]$, is determined by $\theta_l[t] = \omega_l[t]\Delta t$. The updated position of the rod's endpoint, $\mathbf{q}_l^{\mathrm{b}}[t+1]$, is obtained by applying the Rodrigues' rotation formula [21] to the previous position $\mathbf{q}_l^{\mathrm{b}}[t]$ as

$$\mathbf{q}_l^{\mathrm{b}}[t+1] = \mathbf{R}_l(\theta_l[t+1], \mathbf{u}_l[t+1])\mathbf{q}_l^{\mathrm{b}}[t], \tag{1}$$

where $\mathbf{R}_l(\cdot)$ represents the Rodrigues rotation matrix corresponding to the l-th rod. To simplify notation, we define $C_{\theta_l} = \cos\theta_l$, $S_{\theta_l} = \sin\theta_l$, and $D_{\theta_l} = 1 - \cos\theta_l$. With these substitutions, rotation matrix $\mathbf{R}_l(\theta_l, \mathbf{u}_l)$ can be rewritten as

$$\mathbf{R}_l(\theta_l, \mathbf{u}_l) = \begin{bmatrix} C_{\theta_l} + u_x^2 D_{\theta_l} & u_x u_y D_{\theta_l} - u_z S_{\theta_l} & u_x u_z D_{\theta_l} + u_y S_{\theta_l} \\ u_y u_x D_{\theta_l} + u_z S_{\theta_l} & C_{\theta_l} + u_y^2 D_{\theta_l} & u_y u_z D_{\theta_l} - u_x S_{\theta_l} \\ u_z u_x D_{\theta_l} - u_y S_{\theta_l} & u_z u_y D_{\theta_l} + u_x S_{\theta_l} & C_{\theta_l} + u_z^2 D_{\theta_l} \end{bmatrix}. \tag{2}$$

Through (1), we can calculate new vector $\mathbf{q}_l^{\mathrm{b}}[t+1]$ after vector $\mathbf{q}_l^{\mathrm{b}}[t]$ rotates about unit vector $\mathbf{u}_l[t+1]$ by angle $\theta_l[t+1]$. Similarly, a local CCS for the antenna, denoted as $\mathbf{q}_a^{\mathrm{s}}[t+1]$, is established with the connection point between the antenna supporting rod and the 6DMA surface as the origin. In this local CCS, the coordinates of the n-th antenna on the a-th 6DMA surface are represented as $\mathbf{q}_{a,n}^{\mathrm{s}}[t]$. The rotation of the 6DMA surface is characterized by unit vector $\mathbf{u}_a[t]$ and angular velocity $\omega_a[t]$. During time slot t, its rotational transformation corresponding to the a-th 6DMA surface is described by rotation matrix $\mathbf{R}_a(\theta_a[t], \mathbf{u}_a[t])$.

Taking into account the scaling of antenna supporting rod characterized by scaling factor ς_l, the rotation of antenna supporting rod, and the rotation of 6DMA surface, the global position of the n-th antenna on the a-th 6DMA surface at the t-th time slot can be represented by an accumulative control model. The impact of controls at the global and local scales on the global position can be respectively defined as

$$\varsigma_l^{\mathrm{b}}[t] = \prod_{i=1}^{t} \varsigma_l[i], \tag{3}$$

$$\mathbf{R}_l^{\mathrm{b}}[t] = \prod_{i=1}^{t} \mathbf{R}_l(\theta_l[i], \mathbf{u}_l[i]), \tag{4}$$

$$\mathbf{R}_a^{\mathrm{s}}[t] = \prod_{i=1}^{t} \mathbf{R}_a(\theta_a[i], \mathbf{u}_a[i]). \tag{5}$$

Subsequently, the global position of the l-th surface center at time slot t, denoted as $\mathbf{q}_l^{\mathrm{b}}[t]$, is determined by the cumulative scaling and rotation transformations of the supporting rod applied to its initial position, $\mathbf{q}_l^{\mathrm{b}}[0]$, which is given by

$$\mathbf{q}_l^{\mathrm{b}}[t] = \varsigma_l^{\mathrm{b}}[t]\mathbf{R}_l^{\mathrm{b}}[t]\mathbf{q}_l^{\mathrm{b}}[0]. \tag{6}$$

Building on this, since the global CCS and the local CCS share the same scale and initial orientation, for $\forall l = a$, the global position of the n-th antenna element on the a-th surface, $\mathbf{q}_{l,n}^{\mathrm{b}}[t]$, can be obtained by adding the antenna's local coordinate vector, transformed by the surface's own rotation, to its global center position, which is given by

$$\mathbf{q}_{l,n}^{\mathrm{b}}[t] = \mathbf{q}_l^{\mathrm{b}}[t] + \mathbf{R}_a^{\mathrm{s}}[t]\mathbf{q}_{a,n}^{\mathrm{s}}[0], \tag{7}$$

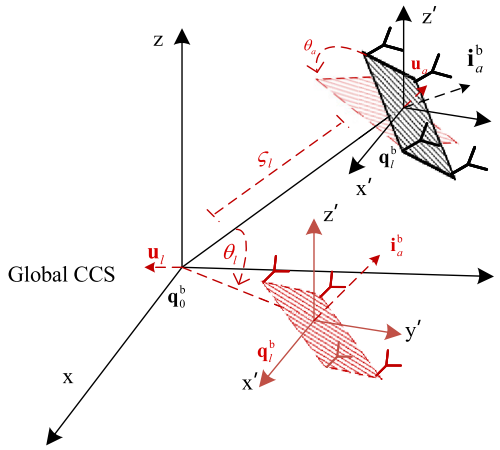

Fig. 2. Schematic of the six DoFs geometric control process for the a-th 6DMA surface, including rod rotation, surface rotation, and telescopic scaling.

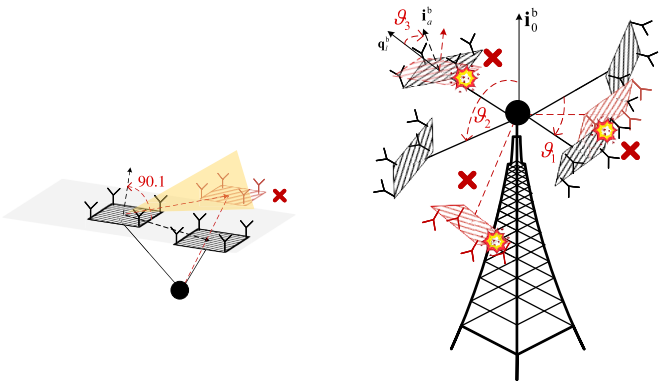

(a) Electromagnetic property constraints

(b) Mechanical structure constraints

Fig. 3. Some constraints during the extension, contraction and rotation of 6DMA surfaces.

where $\mathbf{q}_{a,n}^{\mathrm{s}}[0]$ is the initial position vector of the antenna element in the local coordinate system.

B. Physical Operating Constraints

1) Rotation Constraints to Avoid Signal Reflection: To prevent mutual signal reflections between any two 6DMA surfaces, as depicted in Fig. 3(a), rotational direction constraints must be imposed on every pair of 6DMA surfaces. Under the premise that the local coordinate system of the a-th 6DMA surface is congruent with the global coordinate system in both orientation and scale, the local rotation matrix exerts equivalent influences on both the global and local normal vectors of this surface. For the sequential rotation process of the antenna supporting rod and surface, the transformed normal vector of the a-th 6DMA surface in the global coordinate system can be characterized by the cumulative product of rotation matrices across time slots. Specifically, the expression for the normal vector after sequential rotations is given by

$$\mathbf{i}_a^{\mathrm{b}}[t] = \mathbf{R}_l^e[t]\mathbf{i}_a^{\mathrm{b}}[0]. \tag{8}$$

where the cumulative rotation matrix

$$\mathbf{R}_l^e[t] = \prod_{i=1}^{t} \mathbf{R}_l(\theta_l[i], \mathbf{u}_l[i])\mathbf{R}_a(\theta_a[i], \mathbf{u}_a[i]), \tag{9}$$

encapsulates the cumulative effect of rod rotations and surface rotations on the final orientation of the 6DMA surface over each time slot, and $\mathbf{i}_a^{\mathrm{b}}[0]$ denotes the initial outward unit normal vector at the global reference point.

The hyperplane can be constructed using the center of the a-th 6DMA surface and its outward normal vector in the global coordinate system, and this hyperplane can be expressed as

$$\left\{\mathbf{q}_x^{\mathrm{b}} \mid (\mathbf{i}_a^{\mathrm{b}}[t])^{\mathrm{T}}\mathbf{q}_x^{\mathrm{b}} = (\mathbf{i}_a^{\mathrm{b}}[t])^{\mathrm{T}}\mathbf{q}_l^{\mathrm{b}}[t]\right\}. \tag{10}$$

For any point $\mathbf{q}_x^{\mathrm{b}}$ in space, this hyperplane consists of all points $\mathbf{q}_x^{\mathrm{b}}$ such that vector $\mathbf{q}_x^{\mathrm{b}} - \mathbf{q}_l^{\mathrm{b}}[t]$ is orthogonal to normal vector $\mathbf{i}_a^{\mathrm{b}}[t]$. This hyperplane partitions the 3D space into two halfspaces, one of which is a closed halfspace defined by

$$\left\{\mathbf{q}_x^{\mathrm{b}} \mid (\mathbf{i}_a^{\mathrm{b}}[t])^{\mathrm{T}} \left(\mathbf{q}_x^{\mathrm{b}} - \mathbf{q}_l^{\mathrm{b}}[t]\right) \le 0\right\}. \tag{11}$$

This closed halfspace contains the point $\mathbf{q}_l^{\mathrm{b}}[t]$, and any point $\mathbf{q}_x^{\mathrm{b}}$ within it forms an obtuse or right angle between vector $\mathbf{q}_x^{\mathrm{b}} - \mathbf{q}_l^{\mathrm{b}}[t]$ and normal vector $\mathbf{i}_a^{\mathrm{b}}[t]$. When $\mathbf{q}_x^{\mathrm{b}}$ is set to the center positions of any distinct 6DMA surfaces, for $\forall l \neq l'$ and $l, l' \in \mathcal{L}$, the constraint condition can be formulated as

$$(\mathbf{i}_a^{\mathrm{b}}[t])^{\mathrm{T}} \left(\mathbf{q}_{l'}^{\mathrm{b}}[t] - \mathbf{q}_l^{\mathrm{b}}[t]\right) \le 0. \tag{12}$$

Constraint (12) ensures that the centers of other 6DMA surfaces do not lie within the open halfspace extending along the normal vector direction of the a-th 6DMA surface.

2) Mechanical Structure Constraints: To ensure operational safety and prevent the mechanical collisions depicted in Fig. 3(b), we formulate a set of physical constraints. Direct enforcement of Euclidean distances is computationally intractable as it requires solving complex non-convex subproblems at each optimization step (e.g., minimum distance between noncoplanar rods). We therefore employ a more efficient strategy using geometric angular separations. This method provides a tractable proxy for physical clearance and inherently respects the system's kinematic limits. First, to prevent collisions and coupling between any two 6DMA surfaces, we enforce minimum angular separation ϑ_1 for all surface pairs where $l \neq l'$ and $l, l' \in \mathcal{L}$,

$$\arccos\left(\frac{\mathbf{q}_l^{\mathrm{b}}[t] \cdot \mathbf{q}_{l'}^{\mathrm{b}}[t]}{\left\|\mathbf{q}_l^{\mathrm{b}}[t]\right\| \left\|\mathbf{q}_{l'}^{\mathrm{b}}[t]\right\|}\right) \ge \vartheta_1. \tag{13}$$

Second, to avoid collisions with the main BS structure, minimum angle ϑ_2 is required between each surface and the BS outward normal vector $\mathbf{i}^{\mathrm{b}}[0]$. This constraint applies to all $l \in \mathcal{L}$, which is given by

$$\arccos\left(\left|\frac{\mathbf{q}_l^{\mathrm{b}}[t] \cdot \mathbf{i}^{\mathrm{b}}[0]}{\left\|\mathbf{q}_l^{\mathrm{b}}[t]\right\| \left\|\mathbf{i}^{\mathrm{b}}[0]\right\|}\right|\right) \ge \vartheta_2. \tag{14}$$

Finally, to prevent a surface from colliding with its own supporting rod, minimum angle ϑ_3 must be maintained for all $l \in \mathcal{L}$ where $l = a$,

$$\arccos\left(\left|\frac{\mathbf{q}_l^{\mathrm{b}}[t] \cdot \mathbf{i}_a^{\mathrm{b}}[t]}{\left\|\mathbf{q}_l^{\mathrm{b}}[t]\right\| \left\|\mathbf{i}_a^{\mathrm{b}}[t]\right\|}\right|\right) \ge \vartheta_3. \tag{15}$$

These constraints are defined based on the 6DMA surface centers rather than individual antenna elements. This simplification significantly reduces the number of constraints

and the overall computational complexity, an advantage that is particularly pronounced for large-scale arrays. Although this approach is an approximation, the combination of the halfspace constraint in (12) and the angular separations in (13) through (15) effectively ensures operational safety and mitigates severe signal reflections by maintaining sufficient physical clearance.

C. Channel Model

Throughout the service horizon, the channel response between each 6DMA surface and any UE within the network is jointly determined by both the UE's spatial coordinates and the 6DMA surface's 3D positioning and orientation parameters. In this subsection, we focus on the uplink transmission phase and characterize the channel model governing signal propagation from each UE to all antenna elements distributed across multiple 6DMA surfaces.

1) 6D Steering Vector: For a given time slot t, let $\alpha_{k,j}[t] \in [-\pi/2, \pi/2]$ and $\beta_{k,j}[t] \in [-\pi, \pi]$ denote the elevation and azimuth AOAs of the j-th channel path from the k-th UE at 6DMA-BS's reference position for $1 \le j \le J_k$, where J_k represents the number of received channel paths. The corresponding directional vector in the global coordinate system is

$$\begin{aligned}&\mathbf{f}^{\mathrm{b}}_{k,j}[t]\\&= [\cos\alpha_{k,j}[t]\cos\beta_{k,j}[t],\ \cos\alpha_{k,j}[t]\sin\beta_{k,j}[t],\ \sin\alpha_{k,j}[t]]^{\mathrm{T}}.\end{aligned} \tag{16}$$

The steering vector for the a-th 6DMA surface is determined by the phase differences between its antenna elements and the BS reference position. Given that $\mathbf{q}^{\mathrm{b}}_{l,n}[t]$ is defined by the positional relationships established through scaling and rotation in (7), the phase difference of the n-th antenna element with respect to the BS reference position is $2\pi\left(\mathbf{f}^{\mathrm{b}}_{k,j}[t]\right)^{\mathrm{T}}\mathbf{q}^{\mathrm{b}}_{l,n}[t]/\lambda$, where λ denotes the carrier wavelength. Consequently, the steering vector is expressed as a function of rotational and scaling components as follows

$$\begin{aligned}&\mathbf{v}^{a}_{k,j}\left(\varsigma^{\mathrm{b}}_{l}[t], \mathbf{R}^{\mathrm{b}}_{l}[t], \mathbf{R}^{\mathrm{s}}_{a}[t]\right)\\&= \left[e^{-j\frac{2\pi}{\lambda}\mathbf{f}^{\mathrm{b}}_{k,j}[t]^{\mathrm{T}}\mathbf{q}^{\mathrm{b}}_{l,1}[t]}, \ldots, e^{-j\frac{2\pi}{\lambda}\mathbf{f}^{\mathrm{b}}_{k,j}[t]^{\mathrm{T}}\mathbf{q}^{\mathrm{b}}_{l,n}[t]}\right]^{\mathrm{T}} \in \mathbb{C}^{N\times 1}.\end{aligned} \tag{17}$$

2) Effective Antenna Gain: The effective antenna gain is contingent upon the radiation pattern and the orientation of the 6DMA surface. For the a-th surface, global pointing vector $\mathbf{f}^{\mathrm{b}}_{k,j}[t]$ is projected into its local coordinate system using its rotation matrix, analogous to the formulation in (8), can be expressed as

$$\mathbf{f}^{a}_{k,j}[t] = -\left(\mathbf{R}^{e}_{l}[t]\right)^{\mathrm{T}}\mathbf{f}^{\mathrm{b}}_{k,j}[t] = \left(f^{a,x}_{k,j}[t], f^{a,y}_{k,j}[t], f^{a,z}_{k,j}[t]\right). \tag{18}$$

Note that both $\mathbf{R}_l$ and $\mathbf{R}_a$ are orthogonal matrices, thus, $(\mathbf{R}_l\mathbf{R}_a)^{\mathrm{T}} = (\mathbf{R}_l\mathbf{R}_a)^{-1}$ are used here to simplify calculation. Then the local elevation and azimuth angles can be obtained as

$$\alpha^{a}_{k,j}[t] = \frac{\pi}{2} - \arccos\left(f^{a,z}_{k,j}[t]\right), \tag{19}$$

$$\begin{aligned}\beta^{a}_{k,j}[t] = &\arccos\left(\frac{f^{a,x}_{k,j}[t]}{\sqrt{(f^{a,x}_{k,j}[t])^2 + (f^{a,y}_{k,j}[t])^2}}\right)\\&\times \eta(f^{a,y}_{k,j}[t]),\end{aligned} \tag{20}$$

where $\eta(f^{a,y}_{k,j}[t])$ is a sign function that adjusts the angle calculated by the arccos function based on the sign of the y-component of the vector, defined as

$$\eta(f^{a,y}_{k,j}[t]) = \begin{cases}1, & f^{a,y}_{k,j}[t] \ge 0,\\ -1, & f^{a,y}_{k,j}[t] < 0.\end{cases} \tag{21}$$

According to [22], each antenna element exhibits half-power beamwidths $\alpha_{3\mathrm{dB}}$ and $\beta_{3\mathrm{dB}}$ in the vertical and horizontal dimensions, respectively, where $\alpha_{3\mathrm{dB}} = \beta_{3\mathrm{dB}} = 25°$. Thus, the 3D antenna element gain $G(\alpha^{a}_{k,j}[t], \beta^{a}_{k,j}[t])$ can be determined using (19) and (20) as

$$\begin{aligned}&g^{a}_{k,j}(\alpha^{a}_{k,j}[t], \beta^{a}_{k,j}[t])\\&= g^{\max} - \min\left\{-\left[g_{\mathrm{v}}(\alpha^{a}_{k,j}[t]) + g_{\mathrm{h}}(\beta^{a}_{k,j}[t])\right], \mathfrak{F}\right\},\end{aligned} \tag{22}$$

where $g(\alpha^{a}_{k,j}[t], \beta^{a}_{k,j}[t])$ incorporates both vertical and horizontal radiation patterns, and $g^{\max} = 8$ dBi represents the maximum directional gain of each antenna element in the main lobe direction. The vertical radiation pattern is defined as

$$g_{\mathrm{v}}(\alpha^{a}_{k,j}[t]) = -\min\left\{12\left(\frac{\alpha^{a}_{k,j}[t]}{\alpha_{3\mathrm{dB}}}\right)^2, \mathfrak{S}\right\}, \tag{23}$$

where $\mathfrak{S} = 30$ dBi denotes the sidelobe level limit. The horizontal radiation pattern is given by

$$g_{\mathrm{h}}(\beta^{a}_{k,j}[t]) = -\min\left\{12\left(\frac{\beta^{a}_{k,j}[t]}{\beta_{3\mathrm{dB}}}\right)^2, \mathfrak{F}\right\}, \tag{24}$$

where $\mathfrak{F} = 30$ dBi represents the front-back ratio. Thus, the effective antenna gain corresponding to the a-th 6DMA surface in linear scale is expressed as

$$G^{a}_{k,j}\left(\mathbf{R}^{e}_{l}[t]\right) = 10^{\frac{g\left(\alpha^{a}_{k,j}[t], \beta^{a}_{k,j}[t]\right)}{10}}. \tag{25}$$

3) Effective Channel: When the antenna's physical dimensions or motion range become negligible,[1] the far-field model can be adopted for simplification, assuming that the path response coefficients are identical for all antenna elements corresponding to the same signal propagation path [23], the channel vector between UE k and the BS at t-th time slot can be expressed as

$$\begin{aligned}&\mathbf{h}_k(\boldsymbol{\varsigma}[t], \mathcal{R}^{\mathrm{b}}[t], \mathcal{R}^{\mathrm{s}}[t]) = \sum_{j=1}^{J_k}\mathfrak{P}^{\mathrm{b}}_{k,j}[t]\\&\times\begin{bmatrix}\sqrt{G^{1}_{k,j}\left(\mathbf{R}^{\mathrm{e}}_{1}[t]\right)}\mathbf{v}^{1}_{k,j}\left(\mathbf{R}^{\mathrm{b}}_{1}[t], \mathbf{R}^{\mathrm{s}}_{1}[t]\right)^{\mathrm{T}}\\ \vdots\\ \sqrt{G^{A}_{k,j}\left(\mathbf{R}^{\mathrm{e}}_{L}[t]\right)}\mathbf{v}^{A}_{k,j}\left(\mathbf{R}^{\mathrm{b}}_{L}[t], \mathbf{R}^{\mathrm{s}}_{A}[t]\right)^{\mathrm{T}}\end{bmatrix} \in \mathbb{C}^{AN\times 1}.\end{aligned} \tag{26}$$

[1]Although the 6DMA model offers a larger motion space than 2DMA, the antenna's physical dimensions and motion range are typically still negligible relative to the propagation distance. This is due to the per-slot displacement being constrained by mechanical limits, as well as factors like geometric constraints, a high front-to-back ratio, and the system's objective to maximize spatial multiplexing.

where $\boldsymbol{\varsigma}[t] = [\varsigma_1^{\mathrm{b}}[t], \ldots, \varsigma_L^{\mathrm{b}}[t]]^{\mathrm{T}} \in \mathbb{R}^{L\times 1}$ is the vector of rod scaling factors, while $\mathcal{R}^{\mathrm{b}}[t] = \{\mathbf{R}_l^{\mathrm{b}}[t] \in \mathbb{R}^{3\times 3}\}_{l=1}^{L}$ and $\mathcal{R}^{\mathrm{s}}[t] = \{\mathbf{R}_a^{\mathrm{s}}[t] \in \mathbb{R}^{3\times 3}\}_{a=1}^{A}$ are the sets containing the cumulative rotation matrices for all supporting rods and 6DMA surfaces, respectively. $\mathfrak{P}_{k,j}^{\mathrm{b}}[t]$ is the path gain coefficient of the j-th path from UE k to the reference point in the BS's coverage area.

4) CKM-Enabled Location-Channel Mapping: The CKM essentially constructs a database rooted in the location space, forming a location-channel information mapping system by associating the UE location with channel characteristics. As large-scale propagation parameters determined by the environmental geometric structure and UE location, path gain, AOA, and AoD exhibit sparsity and slow time-variation, rendering it feasible to prestore a discretized angle set within the CKM. Analogous to the angle index graph constructed in [24], a perfect CKM is assumed to exist, which contains the path gain and AOA information for each UE. Consequently, given the all antenna control information, the channel information constructed in (26) can be transformed into a UE specific channel mapping, expressed as

$$\mathbf{h}_k[t] = \mathrm{CKM}(\mathbf{o}_k[t], E[t], \boldsymbol{\varsigma}[t], \mathcal{R}^{\mathrm{b}}[t], \mathcal{R}^{\mathrm{s}}[t]), \tag{27}$$

where $\mathrm{CKM}(\cdot,\cdot)$ denotes the location-channel knowledge mapping function, and $E[t]$ and $\mathbf{o}_k[t]$ represent the environmental information and the location information of UE k at time slot t, respectively. By leveraging the pre-constructed CKM, BSs pre-acquire channel information for all potential paths, transforming traditional real-time feedback-dependent 'blind optimization' into prior-knowledge-based environment-aware communication planning.

III. Problem Formulation and Transformation

A. Problem Formulation

Considering the uplink transmission from the K mobile UEs to the BS, the received signal at the BS in the t-th time slot is given by

$$\mathbf{y}[t] = \mathbf{H}[t]\mathbf{s} + \mathbf{n}, \tag{28}$$

where $\mathbf{H}[t] = [\mathbf{h}_1[t], \mathbf{h}_2[t], \ldots, \mathbf{h}_K[t]] \in \mathbb{C}^{AN\times K}$ denotes the multiple-access channel from K UEs to all 6DMA surfaces at the BS. $\mathbf{s} = \sqrt{p}\,[s_1, s_2, \ldots, s_K]^{\mathrm{T}} \in \mathbb{C}^{K\times 1}$ denotes the transmit signal vector with each s_k denoting the transmit signal of UE k, whose average power is normalized to one and p represents the identical transmit power for all UEs. In (28), $\mathbf{n} \sim \mathcal{CN}(\mathbf{0}_{AN}, \sigma^2\mathbf{I}_{AN})$ is zero-mean additive white Gaussian noise (AWGN) with covariance matrix $\sigma^2\mathbf{I}_{AN}$. From (5) and (9), it can be observed that the effective antenna gain and steering vector at time slot t are collectively determined by all rotational components up to time slot t. Thus, under the conditions of perfect CSI availability at the BS, optimal Gaussian signaling and multiuser joint decoding, the system's sum spectral efficiency can be characterized as [25]

$$\begin{aligned} &C(\boldsymbol{\varsigma}[t], \mathcal{R}^{\mathrm{b}}[t], \mathcal{R}^{\mathrm{s}}[t]) \\ &= \log_2 \det\left(\mathbf{I}_{NA} + \frac{1}{\sigma^2}\sum_{k=1}^{K} p\mathbf{h}_k[t]\mathbf{h}_k[t]^H\right) \\ &= \log_2 \det\left(\mathbf{I}_{NA} + \frac{p}{\sigma^2}\mathbf{H}[t]\mathbf{H}[t]^H\right), \end{aligned} \tag{29}$$

Notably, distinct from traditional FPA systems, the achievable sum spectral efficiency of the 6DMA system is determined by alterations to the effective channel, which are jointly induced by the rotation of the 6DMA surface alongside the rotational-telescopic movements of its supporting rods. To maximize the 6DMA system's service performance throughout the entire operational cycle while ensuring stable system operation, we jointly optimize the telescopic components of antenna supporting rods, the rotational control parameters of antenna supporting rods, and the rotational control parameters of the antenna plane to maximize the spectral efficiency of the 6DMA wireless system. Additionally, physical motion constraints are incorporated to ensure engineering feasibility. Moreover, by leveraging the CKM, we can formulate the trajectory design over the whole service horizon as a unified long-term optimization problem, instead of a series of snapshot-based optimization schemes, thereby highlighting the crucial role of CKM in enabling proactive and physically feasible antenna-trajectory planning. The proposed system's sum spectral efficiency optimization problem is formulated as

$$\max_{\boldsymbol{\varsigma}[t], \mathcal{R}^{\mathrm{b}}[t], \mathcal{R}^{\mathrm{s}}[t]} \quad \sum_{t=1}^{M} C(\boldsymbol{\varsigma}[t], \mathcal{R}^{\mathrm{b}}[t], \mathcal{R}^{\mathrm{s}}[t]) \tag{30a}$$

$$\text{s.t.} \quad 0 \le \omega_l[t] \le \omega^{\mathrm{b,max}}, \quad \forall l \in \mathcal{L}, t \in \mathcal{T}, \tag{30b}$$

$$0 \le \omega_a[t] \le \omega^{\mathrm{s,max}}, \quad \forall a \in \mathcal{L}, t \in \mathcal{T}, \tag{30c}$$

$$\varsigma^{\min} \le \varsigma_l[t] \le \varsigma^{\max}, \quad \forall l \in \mathcal{L}, t \in \mathcal{T}, \tag{30d}$$

$$q^{\mathrm{b,min}} \le \left\|\mathbf{q}_l^{\mathrm{b}}[t]\right\| \le q^{\mathrm{b,max}}, \quad \forall l \in \mathcal{L}, t \in \mathcal{T}, \tag{30e}$$

$$\left\|\mathbf{q}_l^{\mathrm{b}}[t] - \mathbf{q}_l^{\mathrm{b}}[t-1]\right\| \le q^{\mathrm{b},\Delta t}, \ \forall l \in \mathcal{L}, t \in \mathcal{T}, \tag{30f}$$

$$(\mathbf{i}_a^{\mathrm{b}}[t])^{\mathrm{T}}\left(\mathbf{q}_{l'}^{\mathrm{b}}[t] - \mathbf{q}_l^{\mathrm{b}}[t]\right) \le 0, \ \forall l \ne l', l, l' \in \mathcal{L}, t \in \mathcal{T}, \tag{30g}$$

$$\arccos\left(\frac{\mathbf{q}_l^{\mathrm{b}}[t]\cdot\mathbf{q}_{l'}^{\mathrm{b}}[t]}{\left\|\mathbf{q}_l^{\mathrm{b}}[t]\right\|\left\|\mathbf{q}_{l'}^{\mathrm{b}}[t]\right\|}\right) \ge \vartheta_1, \quad \forall l \ne l', l, l' \in \mathcal{L}, t \in \mathcal{T}, \tag{30h}$$

$$\arccos\left(\left|\frac{\mathbf{q}_l^{\mathrm{b}}[t]\cdot\mathbf{i}^{\mathrm{b}}[0]}{\left\|\mathbf{q}_l^{\mathrm{b}}[t]\right\|\left\|\mathbf{i}^{\mathrm{b}}[0]\right\|}\right|\right) \ge \vartheta_2, \ \forall l \in \mathcal{L}, t \in \mathcal{T}, \tag{30i}$$

$$\arccos\left(\left|\frac{\mathbf{q}_l^{\mathrm{b}}[t]\cdot\mathbf{i}_a^{\mathrm{b}}[t]}{\left\|\mathbf{q}_l^{\mathrm{b}}[t]\right\|\left\|\mathbf{i}_a^{\mathrm{b}}[t]\right\|}\right|\right) \ge \vartheta_3, \ \forall l \in \mathcal{L}, l = a, t \in \mathcal{T}, \tag{30j}$$

where $\omega^{\mathrm{b,max}}$ and $\omega^{\mathrm{s,max}}$ represent the maximum angular velocities for the supporting rods and the 6DMA surfaces, respectively. The rod's extension limits are defined by a per-slot scaling factor $[\varsigma^{\min}, \varsigma^{\max}]$ and an overall length range $[q^{\mathrm{b,min}}, q^{\mathrm{b,max}}]$. Constraints (30b)–(30d) ensure the rotational angular velocity of each supporting rod and 6DMA surfaces remains within mechanical limits. Constraint (30e) bounds the spatial domain of 6DMA surface centers to the BS's predefined 3D operational space. By limiting the incremental displacement of each 6DMA surface to a maximum travel distance of $q^{\mathrm{b},\Delta t}$ per time slot, constraint (30f) guarantees smooth, controllable movements and mitigates impractical

position fluctuations. Constraint (30g) uses halfspace projections of surface normals to mitigate inter-surface signal reflections from unfavorable orientations. Geometric constraints (30h)–(30j) enforce minimum angular separations between various antenna components to preclude mechanical collisions and reduce coupling.[2]

The core of problem (30a) lies in maximizing the total system spectral efficiency over the entire period, expressed as a matrix logarithmic determinant function involving multi-dimensional rotational parameter planning. While the logarithmic determinant function is convex under fixed linear channel parameters, the computation of steering vectors and antenna gains relies on trigonometric functions of coupled angular variables and unit vectors, precluding simple convex optimization approaches. Additionally, the dependencies of relative position and normal vector relationships on both the rod's cumulative rotations and the surface's cumulative rotations render the objective function non-convex over the joint space of position and rotation parameters, with complex variable interactions intensifying nonlinearity. Furthermore, geometric constraints (30g)–(30j) involve nonlinear boundaries formed by combinations of dot products, norms, and arccosine functions, which cannot be represented by linear or convex quadratic constraints, introducing additional layers of non-convexity.

B. Problem Transformation

To address the challenges posed by the high-dimensional optimization space, non-convex variables, and complex geometric constraints in the formulated 6DMA optimization problem, we propose a manifold-based optimization framework. Traditional Euclidean-space methods struggle with the non-convexity and high-dimensionality induced by compound rotations, mechanical constraints, and coupled spatiotemporal variables. Instead, leveraging Lie group theory, we reformulate the problem on a product manifold. This structure allows us to treat the rotational DoFs as points on the SO(3) manifold, while the translational DoFs are optimized within their corresponding Euclidean subspaces. This approach aligns with Riemannian optimization principles. Specifically, the rotation matrices we optimize are elements of the SO(3), which is the set of all 3×3 orthogonal matrices with a determinant of 1. As a Lie group, SO(3) constitutes a smooth manifold, making it the natural geometric space for rotation optimization. By treating rotations as points on this SO(3) manifold, we can exploit its intrinsic geometry to avoid the singularities, computational redundancy, and distortion of geometric correlations that plague traditional parameterizations like Euler angles [26]. These factors motivate us to map the problem to an optimization problem on the manifold space. The following sections detail how to represent and solve the problem within the manifold space.

1) Optimization Parameter Smoothing: To handle the optimization parameters, we reframe their optimization by mapping them onto the manifold. For the special orthogonal group SO(3), the geometric characterization of its corresponding Lie algebra $\mathfrak{so}(3)$ can be described as the tangent space at the group identity element $e \in \mathrm{SO}(3)$ [27].

For any $t \in \mathcal{T}$ and $l \in \mathcal{L}$, the rotation parameter set can be expressed as $\mathbf{\Theta}_l[t] \in \mathbb{R}^3$, where $\mathbf{\Theta}_l[t] = \theta_l[t]\mathbf{u}_l[t]$ and $\theta_l[t] = \|\mathbf{\Theta}_l[t]\|$. Through skew-symmetric isomorphism operator $(\cdot)^\times : \mathbb{R}^3 \to \mathfrak{so}(3)$, it is mapped to the Lie algebra form

$$\mathbf{\Theta}_l[t]^\times = \begin{pmatrix} 0 & -\Theta_l^3[t] & \Theta_l^2[t] \\ \Theta_l^3[t] & 0 & -\Theta_l^1[t] \\ -\Theta_l^2[t] & \Theta_l^1[t] & 0 \end{pmatrix} \in \mathfrak{so}(3), \tag{31}$$

where $\mathfrak{so}(3)$ denotes the Lie algebra composed of all third-order skew-symmetric matrices, and $\Theta_l^i[t]$ (for $i = 1, 2, 3$) represents the i-th component of rotation vector $\mathbf{\Theta}_l[t]$. Any element of Lie algebra $\mathbf{\Theta}_l[t]^\times \in \mathfrak{so}(3)$ can be expressed as an element of its Lie group $\mathbf{R}_l(\theta_l[t], \mathbf{u}_l[t]) \in \mathrm{SO}(3)$ through exponential mapping $\exp_{\mathrm{SO}(3)} : \mathfrak{so}(3) \to \mathrm{SO}(3)$, which is defined as

$$\begin{aligned} &\mathbf{R}_l\left(\theta_l[t], \mathbf{u}_l[t]\right) = \exp_{\mathrm{SO}(3)}(\mathbf{\Theta}_l[t]^\times) \\ &= \mathbf{I}_3 + \frac{\sin\theta_l[t]}{\theta_l[t]}\mathbf{\Theta}_l[t]^\times + \frac{1-\cos\theta_l[t]}{\theta_l[t]^2}(\mathbf{\Theta}_l[t]^\times)^2, \end{aligned} \tag{32}$$

where $\theta_l[t] = \|\mathbf{\Theta}_l[t]\|$ denotes the norm of $\mathbf{\Theta}_l[t] \in \mathbb{R}^3$. The logarithm map, $\mathrm{Log}_{\mathrm{SO}(3)} : \mathrm{SO}(3) \to \mathfrak{so}(3)$, as the inverse of the exponential map, maps elements from the special orthogonal group manifold to its Lie algebra, is defined as

$$\begin{aligned} \mathbf{\Theta}_l[t]^\times &= \mathrm{Log}_{\mathrm{SO}(3)}(\mathbf{R}_l\left(\theta_l[t], \mathbf{u}_l[t]\right)) \\ &= \frac{\theta_l[t]}{2\sin\theta_l[t]}(\mathbf{R}_l\left(\theta_l[t], \mathbf{u}_l[t]\right) - \mathbf{R}_l\left(\theta_l[t], \mathbf{u}_l[t]\right)^{\mathrm{T}}), \end{aligned} \tag{33}$$

where

$$\theta_l[t] = \arccos\left(\frac{\mathrm{tr}(\mathbf{R}_l\left(\theta_l[t], \mathbf{u}_l[t]\right)) - 1}{2}\right), \tag{34}$$

$$\mathbf{\Theta}_l[t]^\times = \frac{\theta_l[t]}{2\sin\theta_l[t]}\left((\mathbf{R}_l\left(\theta_l[t], \mathbf{u}_l[t]\right) - \mathbf{R}_l\left(\theta_l[t], \mathbf{u}_l[t]\right)^{\mathrm{T}}\right). \tag{35}$$

Similarly, the surface rotation parameters $(\theta_a[t], \mathbf{u}_a[t])$ can be represented as Lie group element $\mathbf{R}_a[t] \in \mathrm{SO}(3)$ and its corresponding Lie algebra element $\mathbf{\Theta}_a[t]^\times$ in the local CCS via the same mechanism. Another parameter, $\varsigma_l \in \mathbb{R}^+$, for $\forall l \in \mathcal{L}$ can be viewed as a one-dimensional manifold of positive real numbers. In this case, the total parameter space constitutes an unconstrained product manifold, defined as

$$\mathcal{M} := \prod_{t=1}^{T}\prod_{l=1}^{L}\left(\mathbb{R}^+ \times \mathrm{SO}(3) \times \mathrm{SO}(3)\right). \tag{36}$$

Product manifolds preserve smoothness and inherit Riemannian metrics [26]. Subsequently, we can use the notation $x \in \mathcal{M}$ to represent any set of feasible solutions that conform to the manifold structure. This reparameterization is powerful because the orthogonality constraints that define a valid rotation matrix are intrinsically satisfied by the geometry of the SO(3) space. Consequently, the original problem involving complex matrix constraints in Euclidean space is transformed

[2]Since the CKM provides channel states, we assume a quasi-static channel where the antenna movement delay is tolerable.

into an optimization on a manifold where these rotational constraints are handled implicitly by the manifold's structure, significantly simplifying the problem.

2) Restriction Condition Smoothing: While the manifold framework elegantly handles the intrinsic geometric constraints of rotation, our optimization problem (30) is still subject to a set of physical and kinematic inequality constraints. A primary challenge is that these constraints, which govern aspects like collision avoidance and angular velocity limits are inherently non-smooth due to the use of norms and conditional logic. This non-differentiability makes them incompatible with the gradient-based Riemannian optimization methods we aim to use. To resolve this, we reformulate the constrained problem into a smooth, unconstrained problem on the manifold using a smoothed exact penalty measure. Our approach employs a hybrid strategy to handle different constraint types efficiently.

Firstly, for constraints that define simple bounds, we use reparameterization. This approach enforces the constraints by construction, enhancing numerical stability. Specifically, the telescopic scaling factor constraints in (30d) are handled by mapping unconstrained vector $\varsigma_l^m[t] \in \mathbb{R}$ to valid scaling factor $\varsigma_l[t]$ using the transformation

$$\varsigma_l[t] = \varsigma^{\min} + (\varsigma^{\max} - \varsigma^{\min}) \frac{1}{1 + e^{\varsigma_l^m[t]}}, \quad \forall l \in \mathcal{L}. \tag{37}$$

Secondly, for the more complex geometric and kinematic constraints, which denoted by index set $\mathcal{I}_{\text{6DMA}}$, we begin by converting them into standard form $g_i(x) \leq 0$ via simple algebraic transformation. In this form, $g_i(x) > 0$ signifies a violation of the i-th constraint. For instance, the maximum angular velocity constraint $0 \leq \omega_l[t] \leq \omega^{\text{b,max}}$ is reformulated as

$$g_{1,l,t}(x) = -\omega_l[t] \leq 0, \quad \forall l \in \mathcal{L}, \tag{38}$$

$$g_{2,l,t}(x) = \omega_l[t] - \omega^{\text{b,max}} \leq 0, \quad \forall l \in \mathcal{L}. \tag{39}$$

However, the standard exact penalty term, $\max(0, g_i(x))$, is unsuitable because the max operator is non-differentiable. We therefore replace it with its continuously differentiable approximation, the log-sum-exp (LSE) function [28]. For the more complex, state-dependent geometric constraints, we employ a smoothing technique directly on their penalty terms. The constraints in (30e)-(30j) are reformulated as penalty functions as

$$\sum_{i \in \mathcal{I}_{\text{6DMA}}} \rho^i \mu \log\left(1 + e^{g_i(x)/\mu}\right), \quad \forall t \in \mathcal{T}, \tag{40}$$

where $\mu > 0$ is a global smoothing parameter, and $\boldsymbol{\rho}$ is a vector of penalty weights. The selection of these parameters involves a critical trade-off. As $\mu \to 0$, the LSE function more accurately approximates the true penalty, but its gradient becomes numerically unstable. Conversely, as penalty weight $\rho^i \to \infty$, the solution is driven to strictly satisfy the corresponding constraint, but often at the cost of slow convergence or oscillations, as the optimization prioritizes feasibility over objective improvement. Furthermore, the physical constraints considered in this work exhibit significant heterogeneity in dimensionality and scale. A single, uniform penalty weight would be inefficient. To address this multi-scale challenge, our methodology adopts a strategy of independently updating each penalty weight ρ^i within vector $\boldsymbol{\rho}$, allowing for a more tailored and efficient convergence process.

3) Smooth Unconstrained Optimization Problem: By integrating the smoothed penalty terms into the original objective function, the constrained optimization problem in (30) can be reformulated as a smooth unconstrained optimization problem on product manifold $\mathcal{M}$, expressed as

$$\min_{x \in \mathcal{M}} \mathcal{P}(x; \boldsymbol{\rho}, \mu) = -f(x) + \sum_{i \in \mathcal{I}_{\text{6DMA}}} \rho^i \mu \log\left(1 + e^{g_i(x)/\mu}\right), \tag{41}$$

where $\mathcal{P}(x; \boldsymbol{\rho}, \mu)$ denotes the penalized objective function. The LSE approximation ensures that the penalty term is differentiable everywhere on $\mathcal{M}$, enabling the application of Riemannian gradient-based optimization algorithms. Theoretically, if the approximation error from the smoothing function is disregarded, this method functions as an exact penalty measure. Analogous to the Euclidean case, it is a known property on Riemannian manifolds that sufficiently large yet finite penalty weight ρ suffices to make the solution of the penalized problem coincide exactly with that of the original constrained problem [29].

IV. Proposed Solution

A. Tangent Space and Gradient

The optimization problem in (41) is defined on 3D transformation groups, rendering conventional backpropagation via Euclidean embedding unsuitable. Such embeddings introduce singularities, which risk gradient explosion, and inflate the computation graph. We circumvent these issues by employing a backpropagation method that operates directly on the manifold's tangent space. This approach preserves the intrinsic Lie group structure, ensuring numerical stability by avoiding the pitfalls of embedding strategies [30].

Since standard addition and subtraction are not defined for group elements, we must redefine these operations. For any two elements $X, Y \in \mathcal{M}$ and a Lie algebra vector $\xi \in \mathbb{R}^3$, we define them based on the exponential and logarithmic maps from (32) and (33), following the convention in [31] as

$$\oplus : \mathbb{R}^3 \times \mathcal{M} \to \mathcal{M}, \quad \xi \oplus X = \exp(\xi) \circ X, \tag{42}$$

$$\ominus : \mathcal{M} \times \mathcal{M} \to \mathbb{R}^3, \quad X \ominus Y = \log(X \cdot Y^{-1}), \tag{43}$$

where $\oplus$ operator perturbs element X using vector ξ from the Lie algebra, and $\ominus$ maps the difference on the manifold back to the tangent space, $\circ$ is binary operator such that two group elements can be combined to form a third element $X \circ Y \in \mathcal{M}$.

For functions on Lie groups $f : \mathcal{M} \to \mathcal{M}'$, the differential is generalized as a response to perturbations in the tangent space, expressed as

$$Df(X)[\mathbf{v}] = \lim_{t \to 0} \frac{f(t\mathbf{v} \oplus X) \ominus f(X)}{t}, \tag{44}$$

where $\mathbf{v} \in T_X\mathcal{M}$ is a vector in the tangent space at point X. In this context, $Df(X)$ denotes the differential of the map f at X, which is a linear transformation between the respective tangent spaces. This operator maps an infinitesimal perturbation $\mathbf{v}$ in the tangent space of the input X to a

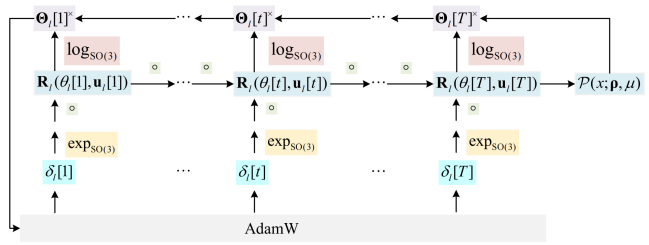

Fig. 4. The update mechanism for a computation graph with Lie group embeddings. Taking the rotation matrix $\mathbf{R}_l(\theta_l[t],\mathbf{u}_l[t])$ from the forward pass as an example, its gradient is not computed in the conventional Euclidean space. Instead, backpropagation and gradient computation are performed within its corresponding tangent space $\boldsymbol{\Theta}_l[t]^\times \in \mathfrak{so}(3)$. The update vector, $\delta_l[t]$, obtained from the optimizer, resides in this tangent space and is subsequently mapped back to the SO(3) manifold via the $\exp_{SO(3)}$ to update $\mathbf{R}_l(\theta_l[t],\mathbf{u}_l[t])$.

corresponding perturbation in the tangent space of the output $f(X)$. Such a formulation generalizes the standard Jacobian matrix, thereby enabling the application of the chain rule for functions defined on manifolds. This equation establishes the mapping from perturbations in the $T_X\mathcal{M}$ to those in the $T_{f(X)}\mathcal{M}$.

Substituting orthonormal basis vectors into (44) yields the Jacobian matrix $\mathbf{J} \in \mathbb{R}^{\dim(\mathcal{M}')\times\dim(\mathcal{M})}$

$$J_{ij} = \lim_{t\to 0} \frac{\langle f(te_j \oplus X) \ominus f(X), e_i' \rangle}{t}, \tag{45}$$

where $\langle\cdot,\cdot\rangle$ denotes an inner product defined on the tangent space of $\mathcal{M}'$. Note that for Euclidean spaces, the exponential and logarithmic maps are identity maps, and the group multiplication $\circ$ degenerates to vector addition. When both inputs and outputs of functions are variables in Euclidean space, (45) aligns with the definition of the standard directional derivative. This framework thus enables simultaneous handling of both scaling and rotational components.

B. Computational Graph and Backpropagation

We model the 6DMA spectral efficiency optimization process as a computation graph, the principle of which is illustrated in Fig. 4. This graph is a hybrid structure, with nodes representing elements from either Euclidean spaces or Lie group manifolds, and edges representing differentiable mappings between them. The implementation leverages LieTorch, a PyTorch library that performs backpropagation directly in the tangent space of each group element, rather than embedding them in a Euclidean space. Optimization is performed using backpropagation to compute gradients. While gradients for Euclidean variables are found using standard partial differentiation, a specialized approach is required for manifold elements. For a function $Y = f(X)$ mapping between manifolds, the gradient of a loss function $\mathcal{L}$ with respect to X is propagated via the chain rule, given by

$$\frac{\partial \mathcal{L}}{\partial X} = \frac{\partial \mathcal{L}}{\partial Y}\frac{\partial Y}{\partial X} = \frac{\partial \mathcal{L}}{\partial Y}\mathbf{J}, \tag{46}$$

where $\frac{\partial \mathcal{L}}{\partial X}$ is a row vector with the same dimension as the tangent space of X, and $\mathbf{J}$ is the Jacobian matrix in (45). (46) computes the Jacobian-vector product.

1) Gradient Propagation Through Group Multiplication: The core challenge in backpropagation through Lie groups stems from the non-commutative nature of group multiplication, which necessitates the adjoint operator to transform tangent space vectors between reference frames. For a Lie group element X, adjoint operator $\mathfrak{A}_X$ is a linear map that relates the right action and left action parameterizations of the tangent space, satisfying

$$X \circ \exp(a) = \exp(\mathfrak{A}_X(a)) \circ X, \tag{47}$$

where a is a tangent space vector in the local coordinate system of X. Specifically, for $X \in$ SO(3), the adjoint operator is the rotation matrix itself, i.e., $\mathfrak{A}_X = X$ [31]. For group multiplication $Z = X \circ Y$ with $X, Y \in$ SO(3), gradient $\frac{\partial \mathcal{L}}{\partial Z}$ is backpropagated to X and Y. The differential with respect to X is

$$\begin{aligned} Df(X)[\mathbf{v}] &= \lim_{t\to 0} \frac{\mathrm{Log}((e^{t\mathbf{v}}XY)(XY)^{-1})}{t} \\ &= \lim_{t\to 0} \frac{\mathrm{Log}(e^{t\mathbf{v}})}{t} = \mathbf{v}. \end{aligned} \tag{48}$$

The differential with respect to Y involves the adjoint operator to handle non-commutativity is

$$\begin{aligned} Df(Y)[\mathbf{v}] &= \lim_{t\to 0} \frac{\mathrm{Log}((Xe^{t\mathbf{v}}Y)(XY)^{-1})}{t} \\ &= \lim_{t\to 0} \frac{\mathrm{Log}(Xe^{t\mathbf{v}}X^{-1})}{t} \\ &= \lim_{t\to 0} \frac{\mathrm{Log}(e^{\mathfrak{A}_X\cdot t\mathbf{v}})}{t} = \mathfrak{A}_X \cdot \mathbf{v}. \end{aligned} \tag{49}$$

Thus, the backpropagated gradients are

$$\frac{\partial \mathcal{L}}{\partial X} = \frac{\partial \mathcal{L}}{\partial Z} \qquad \frac{\partial \mathcal{L}}{\partial Y} = \frac{\partial \mathcal{L}}{\partial Z}\cdot \mathfrak{A}_X. \tag{50}$$

2) Logarithm Map and Tangent Space Gradients: In Euclidean space, the gradient is directly represented as coordinate increments. In the tangent space, however, the gradient must be expressed as a local perturbation on the manifold, and the increment in the tangent space is mapped to the Lie group via the exponential map to achieve parameter updates. Using the exponential map defined in (33) and the differential function defined in (44). For $\phi = \mathrm{Log}(X)$, this process can be expressed as

$$D\,\mathrm{Log}(X)[\mathbf{v}] = \lim_{t\to 0} \frac{\mathrm{Log}(\exp(t\mathbf{v}) \circ X) - \mathrm{Log}(X)}{t}, \tag{51}$$

where $D\,\mathrm{Log}(X)[\mathbf{v}]$ defines the linear map from a perturbation v in the tangent space of X to the resulting change in the Lie algebra, which is the output of the Logarithm map. Then, based on the Baker–Campbell–Hausdorff formula [32], we obtain

$$\lim_{\phi\to 0} \mathrm{Log}(\exp(\delta\xi)\exp(\phi)) \approx \phi + \mathbf{J}_l^{-1}(\phi)\delta\phi. \tag{52}$$

Specifically, for $X \in$ SO(3), $\mathbf{J}_l^{-1}(\phi)$ has a closed-form expression [31], given by

$$\mathbf{J}_l^{-1}(\phi) = \mathbf{I}_{3\times 3} - \frac{1}{2}\hat{\phi} + \left(\frac{1}{\phi^2} - \frac{1+\cos\phi}{2\phi\sin\phi}\right)(\hat{\phi})^2. \tag{53}$$

Finally, the vector in the tangent space can be expressed as

$$\frac{\partial \mathcal{L}}{\partial X} = \frac{\partial \mathcal{L}}{\partial \phi}\cdot \mathbf{J}_l^{-1}(\phi). \tag{54}$$

C. Overall Algorithm

When addressing constrained optimization problems on Riemannian manifolds, the exact penalty measure transforms constraints into an unconstrained problem by introducing penalty terms. However, the selection of the penalty parameter $\boldsymbol{\rho}$ is critical. As stated in [29], when $\boldsymbol{\rho}$ exceeds a certain threshold, the local minimum solution of the penalty function problem coincides with that of the original problem. Since this threshold is often unknown, setting an excessively large initial $\boldsymbol{\rho}$ may deteriorate the condition number and slow down convergence. To resolve this trade-off, our strategy initially prioritizes exploration of the objective function landscape by keeping penalty weights moderate, preventing the optimizer from being prematurely restricted. As the solution converges towards a promising region, the focus then shifts to strict constraint enforcement by systematically increasing the penalty weights to guide the iterate into the feasible set. Therefore, we propose a two-phase adaptive penalty weight update strategy to dynamically balance the merit function and constraint satisfaction. During the warm-up phase, initial penalty weights are allocated based on the proportion of constraint violations, ensuring the constraint terms are of comparable magnitude to the objective function

$$\rho_w^i = \max\left(\rho_{\min}, \min\left(\frac{V^i f(x_w)}{\sum_{i' \in \mathcal{I}_{\text{6DMA}}} V^{i'}}, \rho_{\max}\right)\right), \tag{55}$$

where $V^i = \mu_w log(1 + exp(g_i(x_w)/\mu_w))$ represents the smoothed violation measure for the i-th constraint, and $f(x_w)$ denotes the current objective function value. During the formal phase, the weights are adaptively adjusted based on historical weights ρ_{w-1}^i and the severity of the current constraints as

$$\rho_w^i = \min\left(\rho_{w-1}^i(1+\gamma V^i), \rho_{\max}\right), \tag{56}$$

where γ is the update step length. The smoothing factor μ_w is updated as

$$\mu_{w+1} = max\{\mu_{\min}, \varrho_\mu \mu_w\}, \tag{57}$$

with $\mu_{\min}$ being the minimum allowable value of the smoothing parameter, $\varrho_\mu \in (0,1)$ is the smoothing decay factor.

Since different values of $\boldsymbol{\rho}$ and μ correspond to different solutions, after updating $\boldsymbol{\rho}$ and μ, we regard the newly formed problem as a subproblem. The gradient tolerance determines the precision threshold for the convergence of the optimization algorithms, and its variation directly affects the iteration termination conditions and the accuracy of subproblem solutions. Reducing the gradient tolerance can drive the algorithm to approach stricter stationary points, improving solution accuracy, but it increases the number of iterations and computational time. In the initial iteration stage, the algorithm tends to explore feasible solutions and does not require extremely high solution precision, thus, we adopt a similar dynamic adjustment strategy for gradient tolerance, and this updating process can be expressed as

$$\epsilon_{w+1} = \max\{\epsilon_{\min}, \varrho_\epsilon \epsilon_w\}, \tag{58}$$

where $\varrho_\epsilon \in (0,1)$ is the gradient tolerance decay factor. By leveraging the exponential map (33), the logarithmic mapping (32), and the differential function (51), We can obtain the increment in the tangent space and map it onto the Lie group via the exponential map to achieve parameter updates. Solution x_s for the subproblem can be obtained through the tangent space backpropagation method. The update process can be expressed as

$$x_{s+1} = \exp\left(-\varrho_x \nabla_{\delta_s} \mathcal{P}(x_s; \boldsymbol{\rho}_w, \mu_w)\right) \circ x_s, \tag{59}$$

where $\delta_s = \text{Log}_{\text{SO(3)}}(x_s)$ denotes the logarithmic mapping of x_s, $\nabla_{\delta_s}\mathcal{P}(x_s; \boldsymbol{\rho}_w, \mu_w)$ represents the Riemannian gradient of the penalized objective function with respect to δ_s, and ϱ_x is the learning rate. The iteration of the subproblem terminates when the maximum number of exploration steps is reached or the condition $\|\nabla_{\delta_s}\mathcal{P}(x_{s+1}; \boldsymbol{\rho}_w, \mu_w)\| \le \epsilon_w$ is satisfied.

Algorithm 1 Manifold-Based Spectral Efficiency Optimization With Dynamic Penalty Adjustment

Input: Initial parameters $x_0 \in \mathcal{M}$, initial penalty weights $\boldsymbol{\rho}_0$, initial smoothing factors μ_0, initial gradient tolerance ϵ_0, decay factors $\varrho_\mu, \vartheta_\epsilon \in (0,1)$, minimum values $\mu_{\min}, \epsilon_{\min}$, distance threshold $d_{\min}$, learning rate ϱ_x, and iteration counter s_{max}, w_{max}.

Output: Optimized 6DMA control parameters x^*.

Initialize: Set $x \leftarrow x_0$, $\boldsymbol{\rho} \leftarrow \boldsymbol{\rho}_0$, $\mu \leftarrow \mu_0$, $\epsilon \leftarrow \epsilon_0$, $w = 0$.
repeat
  SET $s = 0$;
  Set warm-start point for subproblem $x_s \leftarrow x_w$;
  repeat
    Compute the logarithmic mapping $\delta_s = \text{Log}_{\text{SO(3)}}(x_s)$ via (33);
    Compute the Riemannian gradient $\nabla_{\delta_s}\mathcal{P}(x_s; \boldsymbol{\rho_w}, \mu_w)$ via (54);
    Update the solution on the manifold $x_{s+1} = \exp(-\varrho_x \nabla_{\delta_s}\mathcal{P}(x_s; \boldsymbol{\rho}_w, \mu_w)) \circ x_s$ via (32);
    Update $s = s + 1$;
  until $||\nabla_{\delta_s}\mathcal{P}(x_{s+1}; \boldsymbol{\rho}_w, \mu_w)|| \le \epsilon_w$ **or** $s > s_{max}$;
  Update iterate $x_w \leftarrow x_{s+1}$;
  Update smoothing factors $\mu_w \leftarrow \max\{\mu_{\min}, \varrho_\mu \mu_w\}$;
  Update penalty weights $\boldsymbol{\rho}_w$ using the two-phase strategy via (55) and (56);
  Update gradient tolerance: $\epsilon_w \leftarrow \max\{\epsilon_{\min}, \vartheta_\epsilon \epsilon_w\}$;
  Update $w = w + 1$;
until $\mathfrak{d}(x_w, x_{w+1}) < d_{\min}$, $\epsilon_w \le \epsilon_{\min}$ **and** $\mu_w \le \mu_{\min}$ **or** $w > w_{max}$;
return $x^* \leftarrow x_{w+1}$.

After each update of $\boldsymbol{\rho}$, ϵ and μ, we continue to optimize x_w with warm-start. The problem is considered approximately solved when the gradient norm satisfies

$$\|\nabla_{\delta_w}\mathcal{P}(x_w, \boldsymbol{\rho}_w, \mu_w)\| \le \epsilon_w, \tag{60}$$

yielding the iterate x_{w+1}. The algorithm terminates when the following conditions are satisfied in the $(w+1)$-th iteration,

$$\mathfrak{d}(x_w, x_{w+1}) < d_{\min}, \tag{61}$$

$$\epsilon_w \le \epsilon_{\min}, \tag{62}$$

$$\mu_w \le \mu_{\min}. \tag{63}$$

where $\mathfrak{d}(x_w, x_{w+1}) = \left\|\mathrm{Log}_{x_w}(x_{w+1})\right\|_{x_w}$ denotes the Riemannian distance between x_w and x_{w+1}, and $\|\cdot\|_{x_w}$ represents the Riemannian norm on the tangent space $T_{x_w}\mathcal{M}$ [27]. This indicates that the problem is approaching a local minimum and the approximate problem sufficiently close to the original. Theoretically, under exact arithmetic, if the minimum step size $d_{\min}$, minimum smoothing parameter $\mu_{\min}$, and minimum gradient tolerance $\epsilon_{\min}$ are all set to 0, and there exists a feasible limit point satisfying the linear independence constraint qualification, this point satisfies the KKT conditions of the original problem [29]. The comprehensive procedure detailed in Algorithm 1, which integrate manifold optimization with an adaptive penalty mechanism to handle complex kinematic constraints, constitutes the core of our proposed solution. For clarity and convenience in the subsequent performance evaluation, we will refer to this overall approach as CKM-enabled kinematically-constrained manifold optimization (KC-MO).

V. Simulation Results

In this section, we evaluate the performance of the proposed 6DMA-BS design and algorithms in maximizing sum spectral efficiency through numerical results. The CKM utilized is generated using the intelligent ray tracing method [33]. Urban maps, including cities such as Ankara and Berlin, are sourced from OpenStreetMap [34]. In the simulated scenario, the heights of UEs, BSs, and buildings are set to 1.5m, 10m, and 25m, respectively. The main simulation parameters are provided in Table I, unless specified otherwise UE mobility patterns are modeled using a random walk approach with varying speeds. All simulations are executed using WinProp software [35], and the presented results are averaged across the four environments to ensure generality. Fig. 5 illustrates an exemplary case of the constructed CKM, detailing its structural format and the encompassed information. In a practical implementation, the proposed framework is envisioned to operate on a central controller, such as the BS's central processing unit or a dedicated edge server. This controller would periodically perform the trajectory optimization by first querying the CKM with predicted UE locations to retrieve channel data for an upcoming service horizon. Subsequently, it would execute Algorithm 1 to compute the optimal and kinematically feasible antenna trajectories, and then dispatch the resulting sequence of target positions and orientations as low-level control commands to the 6DMA actuators. Leveraging the CKM for proactive channel acquisition enables this entire trajectory planning process to be conducted offline, thereby reducing real-time latency constraints and ensuring the viability of the proactive optimization approach.

To emulate a realistic operational scenario, each 6DMA surface is initialized with a random position and orientation within the predefined operational space, and for the sake of clarity, we assume that $\omega^{\mathrm{b,max}} = \omega^{\mathrm{s,max}} = \omega_{\max}$. Due to the adaptive nature of the algorithm, which is characterized by the fact that as the algorithm operates, all penalty weights ρ ultimately tend to ∞ while parameters μ and ϵ tend to 0, the initial values $(\boldsymbol{\rho}_0, \mu_0, \epsilon_0)$ primarily influence the convergence speed. Since optimal initial values are scenario-dependent and best determined empirically, fixed values are not provided here. To validate the effectiveness of our proposed solution, we introduce several benchmark schemes for performance comparison. Among these schemes, those labeled 'Ideal' serve as theoretical upper bounds for performance, as they neglect the antenna's kinematic constraints including limits on angular velocity and telescopic speed. Specifically, the detailed implementation approaches for each benchmark scheme are elaborated as follows.

- **FPA:** The total number of antennas is identical to the other schemes, but they are deployed in a fixed, conventional three-sector configuration. The antennas in each sector are evenly distributed and maintain a standard 15-degree downtilt towards the ground throughout the simulation.

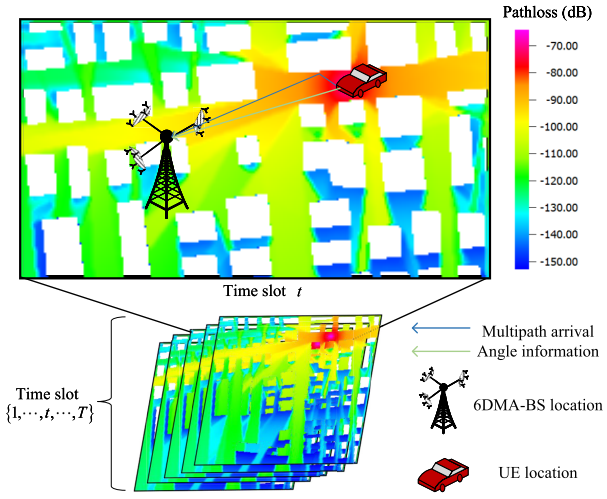

Fig. 5. An example of CKM structure, including UE location, AOA, and path gain mapping.

TABLE I
KEY SIMULATION PARAMETERS

Symbol	Parameter Description	Value
System and Communication Parameters		
Δt	Time slot length	0.5 s
p	Transmit power per UE	200 mW
λ	Carrier wavelength	0.125 m
σ^2	Average noise power	-50 dBm
	UE-BS initial distance range	20 m – 200 m
	UE movement speed	1–6 m/s
6DMA Mechanical Constraints		
J_k	Number of receive channel paths	2
N	Number of antennas per 6DMA surface	4
$[\varsigma^{\min}, \varsigma^{\max}]$	min/max telescopic scaling factor	[0.95,1.05]
$[q^{b,\min}, q^{b,\max}]$	Length range of the supporting rods	[0.8, 1.5] m
$q_l^{b,\Delta t}$	Max. displacement of a surface per time slot	0.3 m
ϑ_1	Min. angle between any two 6DMA surfaces	$\pi/15$ rad
ϑ_2	Min. angle between a surface and the BS structure	$\pi/8$ rad
ϑ_3	Min. angle between a surface and its supporting rod	$\pi/12$ rad

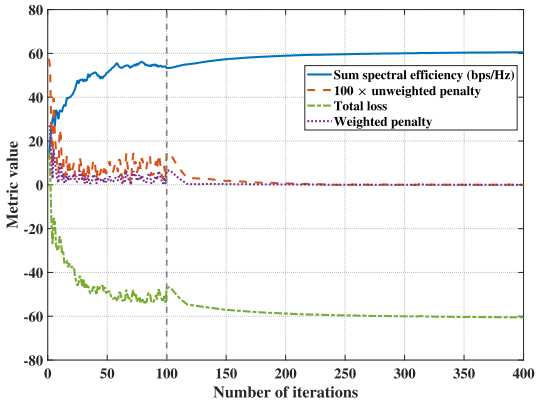

Fig. 6. Convergence of key metrics during the optimization process. The system is configured with a fixed number of $K = 2$ UEs, $M = 10$ time slots and $A = 2$ 6DMA surfaces, with a maximum angular velocity constraint of 0.1 rad/slot.

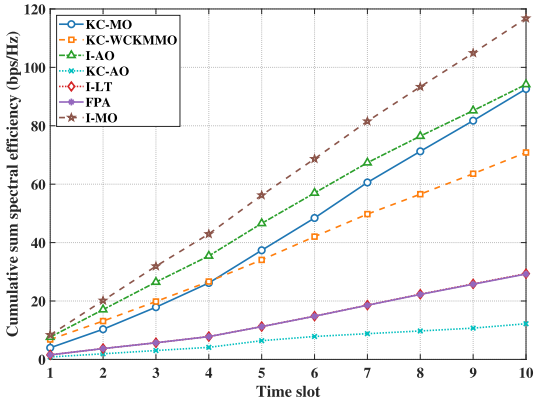

Fig. 7. Comparison of cumulative sum spectral efficiency versus time slot for various antenna orientation strategies. The system is configured with a fixed number of $K = 2$ UEs and $A = 2$ 6DMA surfaces, with a maximum angular velocity constraint of 0.1 rad/slot.

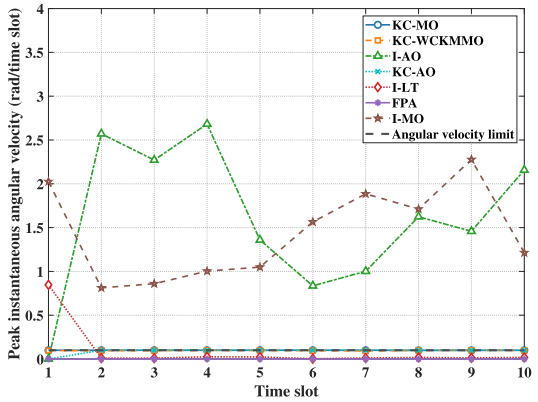

Fig. 8. Peak instantaneous angular velocity versus time slot for different antenna orientation strategies. The system is configured with a fixed number of $K = 2$ UEs and $A = 2$ 6DMA surfaces, with a maximum angular velocity constraint of 0.1 rad/slot.

- **Ideal AO (I-AO):** [6] At each communication time slot, an AO algorithm is used to jointly determine the optimal positions and orientations for all 6DMA surfaces. All constraint parameters are set according to the specifications in [6].
- **Kinematically-constrained AO (KC-AO)**: Computes optimal poses via the AO algorithm at each time slot and then linearly scales the required movement to satisfy the maximum angular velocity constraints.
- **Ideal LoS tracking (I-LT):** At each time slot, the k-means algorithm is used to cluster UEs based on their geographical locations. Each 6DMA surface is associated with a specific UE cluster, and its normal vector is continuously and instantaneously oriented to point towards the geometric centroid of that cluster.
- **Kinematically-constrained without CKM manifold optimization (KC-WCKMMO):** Employs the manifold optimization framework to determine the antenna pose for the next time slot using the CSI from the current time slot.
- **Ideal manifold optimization (I-MO):** Applies the manifold optimization framework without any kinematic constraints on antenna movement.

Fig. 6 illustrates the convergence process of the proposed algorithm in a randomly selected representative simulation, demonstrating its ability to intelligently balance spectral efficiency maximization and constraint satisfaction. In the initial warm-up phase, small penalty weights enable the algorithm to actively explore the solution space, leading to a rapid increase in both system spectral efficiency and transient constraint violation rate. Upon entering the formal optimization phase, the focus of the algorithm shifts to prioritizing feasibility. As the adaptive penalty weights increase, the constraint violation rate decreases rapidly, with only a slight and controlled trade-off in spectral efficiency. This phenomenon confirms that the adaptive penalty mechanism successfully guides the optimization process towards a solution that is not only high-performing but also robust and physically feasible.

Fig. 7 and Fig. 8 illustrate the comparative performance of the schemes. The static FPA and I-LT methods form a baseline performance bound, as their inability to adapt to the true multipath channel structure prevents them from exploiting available spatial DoFs. The reactive KC-WCKMMO scheme initially performs well but suffers a sharp decline, a consequence of its myopic optimization strategy. This approach leads to suboptimal antenna poses from which recovery is kinematically infeasible. In contrast, while the unconstrained I-AO exhibits superior theoretical performance, its required angular velocities are physically challenging to realize. This makes the I-AO scheme difficult to apply in practical systems. The KC-AO scheme, which enforces constraints by linearly scaling the trajectory, results in performance even worse than the static baseline. Our proposed KC-MO framework, however, successfully achieves near-optimal results comparable to the I-AO scheme while remaining strictly within all engineering constraints. This is attributed to its end-to-end manifold optimization, which holistically solves the trajectory problem without the performance loss incurred by iterative approximations or naive constraint handling.

As shown in Fig. 9, increasing the number of UEs K enhances the sum spectral efficiency for all schemes due to

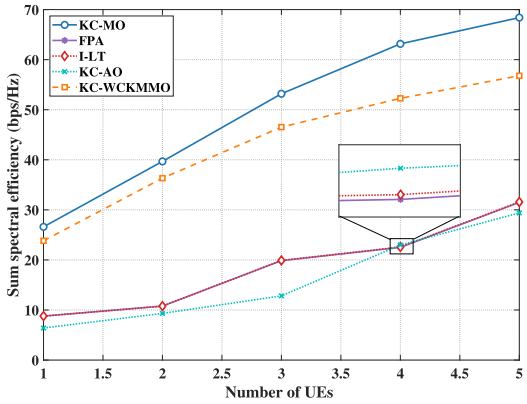

Fig. 9. Sum spectral efficiency versus the number of UEs K for different strategies. The system is configured with a fixed number of $M = 4$ time slots and $A = 3$ surfaces, with a maximum angular velocity constraint of 0.25 rad/slot.

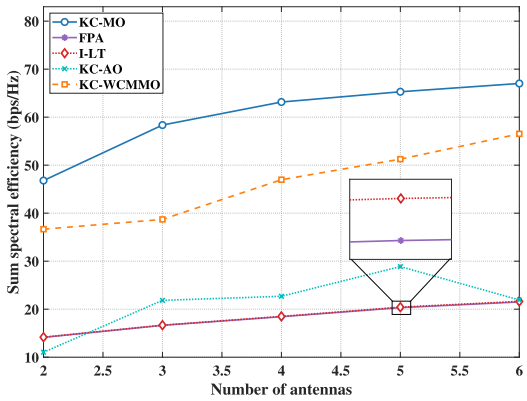

Fig. 10. Sum spectral efficiency versus the number of 6DMA surfaces A for different strategies. The system is configured with a fixed number of $M = 4$ time slots and $K = 3$ UEs, with a maximum angular velocity constraint of 0.25 rad/slot.

multi-user diversity. Crucially, the performance gap between our proactive KC-MO and the reactive KC-WCKMMO widens with K. The increasing channel complexity amplifies the penalty of KC-WCKMMO's myopic decisions, as kinematic constraints make it progressively harder to correct for past suboptimal poses. In contrast, the performance of I-LT and KC-AO fluctuates irregularly, as these methods lack the adaptability to consistently exploit the spatial DoFs in dense UE scenarios. This result highlights the superior robustness and scalability of the proposed KC-MO algorithm. Notably, while the rate of spectral efficiency increase for FPA grows steadily with the number of UEs, the growth rate for KC-MO shows a slowing trend. This suggests that our proactive scheme is more significantly advantageous for scenarios focused on providing high-quality service to a small number of targets.

Fig. 10 shows that while increasing the number of 6DMA surfaces A boosts performance across all schemes, the degree of improvement varies significantly. Baseline methods like I-LT and KC-AO show only marginal or irregular gains, failing to effectively leverage the additional DoFs. Notably, the performance gap between KC-MO and KC-WCKMMO exhibits a non-monotonic trend. At lower values of A, KC-MO's long-term planning provides a distinct advantage in the resource-constrained environment. As A becomes large, the abundance of DoFs allows even the myopic KC-WCKMMO to find effective configurations with less kinematic effort, thereby narrowing the gap.This dynamic underscores the high spatial resource efficiency of our proposed framework, particularly in complex, kinematically constrained scenarios, confirming that an advanced optimization algorithm is key to delivering tracking coverage services with maximal efficiency.

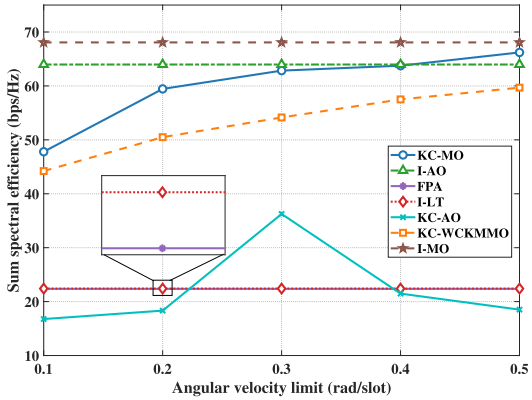

Fig. 11. Sum spectral efficiency versus the maximum angular velocity limit $\omega_{\max}$ for different strategies. The system is configured with a fixed number of $A = 3$ surfaces, $M = 5$ time slots and $K = 4$ UEs.

Fig. 11 reveals the impact of the maximum angular velocity limit $\omega_{\max}$ on system performance. The performance of our proposed KC-MO scheme improves as $\omega_{\max}$ increases, with the gains tapering off at higher velocities. This indicates that once the system possesses sufficient agility to track the optimal channel variations, further increases in velocity yield diminishing marginal returns. In stark contrast, the performance of the myopic KC-WCKMMO scheme shows a near-linear improvement. This reactive strategy continuously leverages higher mobility to compensate for its short-sighted decisions from previous time slots. Meanwhile, the KC-AO scheme's performance remains poor and erratic, as its naive trajectory truncation method consistently fails to yield a coherent or effective path. Ultimately, these results confirm that our KC-MO framework achieves near-optimal performance with moderate velocity limits, allowing designers to use cost-effective actuators and avoid over-engineering, thereby balancing system cost and capability.

VI. Conclusion

In this paper, to address the challenge of proactive UE tracking, we have proposed a long term trajectory optimization method for a 6DMA-enabled BS, leveraging a CKM for predictive channel information. We formulated the problem of maximizing sum spectral efficiency while incorporating the complex kinematics of the 6DMA and a comprehensive set of physical constraints. To solve this challenging non-convex problem, we developed a novel manifold optimization framework that operates on the SO(3) Lie group, using an adaptive

penalty algorithm based on tangent space backpropagation. Our extensive simulation results have validated the superior performance of the proposed method. Compared to benchmark schemes, including conventional FPA, I-AO, KC-AO, I-LT and KC-WCKMMO, our KC-MO demonstrated a significant enhancement in cumulative sum spectral efficiency. Crucially, this performance gain is achieved while strictly adhering to all kinematic and engineering constraints, resulting in smooth and physically feasible antenna trajectories. This work explores the feasibility of channel knowledge map-enabled 6DMA systems with kinematic constraints. Our results offer valuable insights into the potential performance gains and provide a theoretical benchmark for future research on the practical implementation of 6DMA systems.

REFERENCES

[1] R. Sun et al., "A comprehensive survey of knowledge-driven deep learning for intelligent wireless network optimization in 6G," *IEEE Commun. Surveys Tuts.*, early access, May 29, 2025, doi: 10.1109/COMST.2025.3574765.

[2] R. Sun, N. Cheng, C. Li, F. Chen, and W. Chen, "Knowledge-driven deep learning paradigms for wireless network optimization in 6G," *IEEE Netw.*, vol. 38, no. 2, pp. 70–78, Mar. 2024.

[3] C. Wang, Z. Li, K.-K. Wong, R. Murch, C.-B. Chae, and S. Jin, "AI-empowered fluid antenna systems: Opportunities, challenges, and future directions," *IEEE Wireless Commun.*, vol. 31, no. 5, pp. 34–41, Oct. 2024.

[4] L. Zhu, W. Ma, and R. Zhang, "Movable antennas for wireless communication: Opportunities and challenges," *IEEE Commun. Mag.*, vol. 62, no. 6, pp. 114–120, Jun. 2024.

[5] C. Dou, Y. Wu, L. Qian, K.-K. Wong, and T. Q. S. Quek, "Fluid antenna empowered integration of sensing, communications and computing with hybrid multi-task offloading," *IEEE Wireless Commun. Lett.*, vol. 14, no. 8, pp. 2521–2525, Aug. 2025.

[6] X. Shao, Q. Jiang, and R. Zhang, "6D movable antenna based on user distribution: Modeling and optimization," *IEEE Trans. Wireless Commun.*, vol. 24, no. 1, pp. 355–370, Jan. 2025.

[7] X. Shao and R. Zhang, "6DMA enhanced wireless network with flexible antenna position and rotation: Opportunities and challenges," *IEEE Commun. Mag.*, vol. 63, no. 4, pp. 121–128, Apr. 2025.

[8] X. Shao et al., "A tutorial on six-dimensional movable antenna for 6G networks: Synergizing positionable and rotatable antennas," 2025, *arXiv:2503.18240*.

[9] W. Ma, L. Zhu, and R. Zhang, "MIMO capacity characterization for movable antenna systems," *IEEE Trans. Wireless Commun.*, vol. 23, no. 4, pp. 3392–3407, Apr. 2024.

[10] L. Zhu, W. Ma, B. Ning, and R. Zhang, "Movable-antenna enhanced multiuser communication via antenna position optimization," *IEEE Trans. Wireless Commun.*, vol. 23, no. 7, pp. 7214–7229, Jul. 2024.

[11] G. Hu et al., "Fluid antennas-enabled multiuser uplink: A low-complexity gradient descent for total transmit power minimization," 2023, *arXiv:2312.05763*.

[12] W. Lyu, S. Yang, Y. Xiu, Z. Zhang, C. Assi, and C. Yuen, "Movable antenna enabled integrated sensing and communication," *IEEE Trans. Wireless Commun.*, vol. 24, no. 4, pp. 2862–2875, Apr. 2025.

[13] S. Peng et al., "Joint antenna position and beamforming optimization with self-interference mitigation in movable antenna aided ISAC system," in *Proc. IEEE Wireless Commun. Netw. Conf. (WCNC)*, Mar. 2025, pp. 1–6.

[14] Z. Feng, Y. Zhao, K. Yu, and D. Li, "Movable antenna empowered physical layer security without Eve's CSI: Joint optimization of beamforming and antenna positions," 2024, *arXiv:2405.16062*.

[15] X. Shao, R. Zhang, Q. Jiang, J. Park, T. Q. S. Quek, and R. Schober, "Distributed channel estimation and optimization for 6D movable antenna: Unveiling directional sparsity," *IEEE J. Sel. Topics Signal Process.*, vol. 19, no. 2, pp. 349–365, Mar. 2025.

[16] Z. Xiao, X. Pi, L. Zhu, X.-G. Xia, and R. Zhang, "Multiuser communications with movable-antenna base station: Joint antenna positioning, receive combining, and power control," *IEEE Trans. Wireless Commun.*, vol. 23, no. 12, pp. 19744–19759, Dec. 2024.

[17] J. Wu et al., "Low-altitude wireless networks: A comprehensive survey," 2025, *arXiv:2509.11607*.

[18] A. C. P. K. Siriwardhana, J. Yuan, and Z. Shen, "Optimizing handover mechanism in vehicular networks using deep learning and optimization techniques," *Comput. Netw.*, vol. 270, Oct. 2025, Art. no. 111488.

[19] X. Shao, R. Zhang, Q. Jiang, and R. Schober, "6D movable antenna enhanced wireless network via discrete position and rotation optimization," *IEEE J. Sel. Areas Commun.*, vol. 43, no. 3, pp. 674–687, Mar. 2025.

[20] Y. Zeng et al., "A tutorial on environment-aware communications via channel knowledge map for 6G," *IEEE Commun. Surveys Tuts.*, vol. 26, no. 3, pp. 1478–1519, 3rd Quart., 2024.

[21] J. S. Dai, "Euler–Rodrigues formula variations, quaternion conjugation and intrinsic connections," *Mechanism Mach. Theory*, vol. 92, pp. 144–152, Oct. 2015.

[22] *Technical Specification Group Radio Access Network; Study on 3D Channel Model for LTE*, document TR 36.873 V12.4.0, 3GPP, Dec. 2017.

[23] L. Zhu, W. Ma, and R. Zhang, "Modeling and performance analysis for movable antenna enabled wireless communications," *IEEE Trans. Wireless Commun.*, vol. 23, no. 6, pp. 6234–6250, Jun. 2024.

[24] D. Wu, Y. Zeng, S. Jin, and R. Zhang, "Environment-aware hybrid beamforming by leveraging channel knowledge map," *IEEE Trans. Wireless Commun.*, vol. 23, no. 5, pp. 4990–5005, May 2024.

[25] D. Tse and P. Viswanath, *Fundamentals of Wireless Communication*. Cambridge, U.K.: Cambridge Univ. Press, 2005.

[26] H. Sato, *Riemannian Optimization and Its Applications*, vol. 670. Cham, Switzerland: Springer, 2021.

[27] N. Boumal, *An Introduction to Optimization on Smooth Manifolds*. Cambridge, U.K.: Cambridge Univ. Press, 2023.

[28] C. Chen and O. L. Mangasarian, "Smoothing methods for convex inequalities and linear complementarity problems," *Math. Program.*, vol. 71, no. 1, pp. 51–69, Nov. 1995.

[29] C. Liu and N. Boumal, "Simple algorithms for optimization on Riemannian manifolds with constraints," *Appl. Math. Optim.*, vol. 82, no. 3, pp. 949–981, Dec. 2020.

[30] Z. Teed and J. Deng, "Tangent space backpropagation for 3D transformation groups," in *Proc. IEEE/CVF Conf. Comput. Vis. Pattern Recognit. (CVPR)*, Jun. 2021, pp. 10333–10342.

[31] J. Sola, J. Deray, and D. Atchuthan, "A micro lie theory for state estimation in robotics," 2018, *arXiv:1812.01537*.

[32] T. D. Barfoot, *State Estimation for Robotics*. Cambridge, U.K.: Cambridge Univ. Press, 2024.

[33] T. Rautiainen, G. Wolfle, and R. Hoppe, "Verifying path loss and delay spread predictions of a 3D ray tracing propagation model in urban environment," in *Proc. IEEE 56th Veh. Technol. Conf.*, vol. 4, Feb. 2002, pp. 2470–2474.

[34] OpenStreetMap Contributors. (2017). *Planet Dump*. [Online]. Available: https://www.openstreetmap.org

[35] R. Hoppe, G. Wolfle, and U. Jakobus, "Wave propagation and radio network planning software WinProp added to the electromagnetic solver package FEKO," in *Proc. Int. Appl. Comput. Electromagn. Soc. Symp. Italy (ACES)*, Mar. 2017, pp. 1–2.